Journal of Computational Physics 229 (2010) 6027–6046

Contents lists available at ScienceDirect

Journal of Computational Physics

journal homepage: www.elsevier.com/locate/jcp

L^∞-stability of vertex-based MUSCL finite volume schemes on unstructured grids: Simulation of incompressible flows with high density ratios

Caterina Calgaro [a,b], Emile Chane-Kane [b], Emmanuel Creusé [a,b,*], Thierry Goudon [a,b]

[a] Laboratoire Paul Painlevé, UMR 8524, C.N.R.S.-Université Lille 1, Sciences et Technologies, Cité Scientifique, F-59655 Villeneuve d'Ascq cedex, France
[b] EPI SIMPAF, Centre de Recherche INRIA Lille Nord Europe, Parc Scientifique de la Haute Borne, Avenue Halley B.P. 70478, F-59658 Villeneuve d'Ascq cedex, France

ARTICLE INFO

Article history:
Received 1 August 2009
Received in revised form 19 April 2010
Accepted 20 April 2010
Available online 29 April 2010

Keywords:
Finite volume method
Maximum principle property
Variable density flows
Unstructured meshes

ABSTRACT

This work is devoted to the design of multi-dimensional finite volume schemes for solving transport equations on unstructured grids. In the framework of MUSCL vertex-based methods we construct numerical fluxes such that the local maximum property is guaranteed under an explicit Courant–Friedrichs–Levy condition. The method can be naturally completed by adaptive local mesh refinements and it turns out that the mesh generation is less constrained than when using the competitive cell-centered methods. We illustrate the effectiveness of the scheme by simulating variable density incompressible viscous flows. Numerical simulations underline the theoretical predictions and succeed in the computation of high density ratio phenomena such as a water bubble falling in air.

1. Introduction

We are concerned with the numerical simulation of the advection of a scalar quantity: given a velocity field $\mathbf{u} \in \mathbb{R}^N$, depending on the time and space variables $(t,\mathbf{x}) \in \mathbb{R}^+ \times \mathbb{R}^N$, we wish to compute the solution $\rho(t,\mathbf{x}) \in \mathbb{R}$ of

$$\partial_t \rho + \mathrm{div}_{\mathbf{x}}(\rho \mathbf{u}) = 0. \tag{1}$$

To this end, we shall use finite volume methods which are quite natural to this problem since they are based on the conservation relation

$$\frac{\mathrm{d}}{\mathrm{d}t}\int_C \rho(t,\mathbf{x})\mathrm{d}\mathbf{x} = -\int_{\partial C} \rho \mathbf{u}\cdot\mathbf{n}(\mathbf{x})\mathrm{d}\sigma(\mathbf{x})$$

which holds for any subdomain C. Therefore, the method is based on a suitable definition of the fluxes on the interfaces of the control volumes C that realize a tessellation of the whole computational domain. Anticipating on precise definitions, we distinguish among these methods between the vertex-based methods where variables are stored at the mesh vertices and cell-centered methods where variables are stored at the centroids of the cells. For a given mesh, there are many more degrees of freedom for a cell-center scheme than with a vertex-based scheme, but the structure of the discrete operators is more sparse. In particular, for a given number of unknowns, a fixed vertex has more neighbors than a fixed cell, which could lead to expect

* Corresponding author at: Laboratoire Paul Painlevé, UMR 8524, C.N.R.S.-Université Lille 1, Sciences et Technologies, Cité Scientifique, F-59655 Villeneuve d'Ascq cedex, France.
E-mail addresses: Caterina.Calgaro@math.univ-lille1.fr (C. Calgaro), Chane-Kane@inria.fr (E. Chane-Kane), Emmanuel.Creuse@math.univ-lille1.fr (E. Creusé), Thierry.Goudon@inria.fr (T. Goudon).

0021-9991/$ - see front matter © 2010 Elsevier Inc. All rights reserved.
doi:10.1016/j.jcp.2010.04.034

more accuracy with a vertex-based approach. However, while it might be natural to define the most effective discretization as the one which provides the highest accuracy at the lowest cost, the comparison between the two possible discretizations remains difficult and there is no conclusive answer. This is due to the difficulty in defining an appropriate notion of "equivalent mesh". We refer to [32] for an attempt in this direction, considering transonic flows. We also refer to [34] for a complete commented overview of the debate on the pros and cons of these methods. In this work, we find some advantages in working in the vertex-based framework. Our first motivation comes from the development of hybrid finite volume/finite element schemes for the simulation of variable density viscous flows as introduced in [11], for which it is convenient to use a vertex-based approximation of the density since it naturally defines on cells a $\mathbb{P}1$ approximation of the density to be used for treating the momentum equation. Furthermore, for such simulations, due to the coupling between the density and the velocity field, it is crucial to use a scheme for (1) that preserves the maximum principle. This is the main issue devised in this paper. As it will be shown below, it turns out that L^∞ stability on unstructured meshes can be justified for vertex-based meshes under less restrictive geometric assumptions than for cell-center methods.

The problem we address faces two difficulties:

- Firstly, as it is well-known numerical approximation of (1) might generate diffusion and smooth out steep gradients. When dealing with multi-dimensional problems, as pointed in [23,22], the origin of numerical diffusion is twofold. Additionally to the usual diffusion in the direction of the velocity field, which already occurs in dimension one, diffusion phenomena also arise in transverse directions when the mesh is not aligned with the velocity.
- Secondly, we wish to work with unstructured grids. However, removing the Cartesian geometry of the mesh induces a loss of consistency: order one methods do not satisfy order one estimates on unstructured meshes. Fine analysis of this phenomenon can be found in [20,21,36,35,18].

The necessity to consider unstructured meshes can be motivated as follows. On the one hand, removing structure constraints make easier the tiling of complex geometries. On the other hand, bearing in mind complex and multi-physics problems, we realize that meshing uniformly on the finest scales is definitely non-affordable. Then, we wish to couple the scheme with adaptive mesh refinements strategies which make the grids finer close to large gradients. The use of automated mesh generation produces unstructured grids. However, it might be difficult when using such refinements methods to respect the strong geometrical constraints which usually appear in the proof of stability statements. Finally, we address as a requirement for the scheme to preserve the local maximum principle satisfied by the solutions of (1). The motivation in preserving L^∞ estimates and the maximum principle is twofold. First of all the conservation of extrema can be considered as a fundamental physical property of the equation that a numerical scheme must reproduce (a mass or a temperature density should be positive). This is particularly crucial if one thinks of the transport equation as part of a more complex and coupled problem where the violation of the maximum principle might lead to definition troubles. Second of all spurious oscillations can lead, especially in coupled systems where ρ becomes a data for determining the evolution of the velocity, to severe stability issues. We shall illustrate all these aspects with the simulation of variable density incompressible viscous flows, by using the hybrid finite volume/finite element scheme introduced in [11]. The difficulty of such problems is embodied into two dimensionless parameters: the Reynolds number and the ratio between the densities of the heavy and the light fluids. The larger these numbers, the more difficult the problem. The method we discuss is well-suited to be used with the scheme of [11] and we shall show that we can indeed consider high density ratios.

Clearly, a simple first order upwind method cannot produce satisfactory results and, anyway, useful engineering calculations generally require second-order spatial accuracy. Hence, a possible avenue consists in increasing the order of approximation by constructing piecewise linear approximations of the unknown. However, high order methods might have a bad behavior when the solution presents strong variations. Motivated by the *BV* estimate satisfied by the solutions of scalar conservation laws, limiters can be defined in order to restore the TVD property of the scheme [29] and so to prevent the solution from non-physical oscillations near the discontinuities of the solution. It avoids under and overshoots phenomena and it can lead in particular to a maximum principle on the discrete solution. This is the spirit of Monotone Upstream Scheme for Conservation Law (MUSCL) methods as introduced by Van Leer with the one-dimensional analysis of the resolution of hyperbolic conservation laws [44]. Since then, the MUSCL technique has become a standard, used in many academic and industrial codes, see e.g. [34]. A large bibliography database is devoted to the development of several one-dimensional limiters, and the study of the corresponding schemes convergence [39,43,45,37,46]. Unfortunately, the generalization of this approach for multi-dimensional problems is not straightforward at all. A first obstruction comes from the negative result of [27] which establishes that any multi-dimensional TVD scheme is at most first-order accurate.[1] Next, the way to determine the gradients involved in the reconstruction of the solution at the interfaces of a given control volume, having in mind to satisfy the maximum principle, is not a so easy task. Alternative approaches have been proposed. The Essentially Non Oscillatory scheme, see e.g.

[1] The precise result we have in mind states that *any two-dimensional FV scheme of the form*

$$u_{ij}^{n+1} = u_{ij}^n - \frac{\Delta t}{|T_{ij}|}\left(g_{i+1/2,j}^n - g_{i-1/2,j}^n + h_{i,j+1/2}^n - h_{i,j-1/2}^n\right)$$

with Lipschitz-continuous numerical fluxes $g_{i+1/2,j} = g(u_{i-p,j-q},\ldots,u_{i+r,j+s})$, $h_{i+1/2,j} = h(u_{i-p,j-q},\ldots,u_{i+r,j+s})$, which verifies $TV(u^{n+1}) \leqslant TV(u^n)$ is at most first-order accurate, see e.g. Th. 3.7 in [4].

[41,17], is particularly adapted to Cartesian grids. It uses a large stencil and therefore it is not so convenient in a local mesh refinement context. Subject to recent developments, a promising approach is the Residual Distributed Method as discussed in [2]. It is also worth mentioning the work [22] which adopts a different viewpoint since, contrarily to the MUSCL method, the approximation remains discontinuous over the cells. In [22] the direction of the velocity is privileged for the construction of the fluxes which furthermore is based on anti-dissipative strategies. The method is shown to be L^∞ stable under a CFL condition comparable to the one that will be discussed below.

The first attempts to develop efficient MUSCL methods on multi-dimensional unstructured grids were concerned with the design of slope limiting procedures for cell-centered schemes dealing with grids made of triangles by the use of "monoslope" limiters [5,24,33,6]. It consists in defining on each control volume a certain gradient, which is used to generate a linear reconstruction of the solution at the interfaces of this control volume, and then to limit it in order to ensure the local maximum principle. Monoslope limiters for vertex-based methods have been also proposed, see e.g. [19], with applications in aerodynamics, but the most refined limiters strategies have been designed for cell-centered schemes. An elaborate improvement which takes more into account the multi-dimensional aspects of the problem is due to [30]. Very recently, a "multislope" variant has been proposed first for two-dimensional problems [9] and then extended to dimension three [16]. In these methods, the numerical gradient depends not only on the control volume under consideration, but also on the interfaces of the control volume. In the same vein, it is also possible to design a scheme which does not necessarily reduce to order one near extrema. In counterparts the scheme does not always satisfy a maximum principle any more. We refer to [13] which proposes a new reconstruction inspired by ENO. However, the stability investigated in [13] relies on geometrical constraint related to the finite speed of propagation and the L^∞ stability is not obtained. Nevertheless, this can be enough to obtain stable computations according to the physical problem under consideration and the numerical experiments are indeed very convincing. Note also that proving the L^∞ stability of the multislope cell-centered scheme needs geometrical constraints on the mesh, which can be difficult to verify by automated generation, especially in dimension three, see [3] where another variant is proposed from [9,16]. In the present paper, strongly inspired by [15], a multi-dimensional flux limiter strategy is considered for the resolution of (1). However, by contrast to the mentioned references, we deal with vertex-based schemes instead of cell-centered schemes. In this context, it turns out that we are able to propose a gradient reconstruction for which the L^∞ stability can be justified provided a (explicit) Courant–Friedrichs–Levy condition is fulfilled. The proof works for divergence free velocity field, not necessarily constant. Furthermore, the stability is obtained without the restrictive geometrical requirements needed for the cell-centered methods. Numerical tests show the robustness and the accuracy of the numerical method we derive. In particular this treatment of the mass conservation equation allows to consider high density ratio when simulating multicomponent incompressible viscous flows.

The schedule of the paper is the following. In Section 2, we explain our motivation that comes from the simulation of incompressible Navier–Stokes equations with inhomogeneous density. We briefly recall the governing equations as well as the numerical scheme introduced in [11]. Then, we detail the vertex-based finite volume scheme we propose for solving (1), with a multislope gradient reconstruction. In Section 3, we establish the maximum principle property for the scheme under an explicitly given CFL condition. Finally, Section 4 is devoted to numerical results and we make comparisons with other simulations in recent bibliography. Three classical benchmark test cases are addressed: the translated field, the rotational field and the falling droplet.

2. Motivation and description of the numerical scheme

2.1. Density dependent Navier–Stokes equations and time discretization

Our motivation comes from the simulation of the variable density incompressible Navier–Stokes system. From now on, Ω stands for an open bounded polygonal subset on $\mathbb{R}^2$. We are interested in the following PDEs system

$$\partial_t \rho + \mathrm{div}_{\mathbf{x}}(\rho \mathbf{u}) = 0, \tag{2}$$

$$\partial_t(\rho \mathbf{u}) + \mathrm{Div}_{\mathbf{x}}(\rho \mathbf{u} \otimes \mathbf{u}) + \nabla_{\mathbf{x}} p - \mu \Delta_{\mathbf{x}} \mathbf{u} = \mathbf{f}, \tag{3}$$

$$\mathrm{div}_{\mathbf{x}} \mathbf{u} = 0. \tag{4}$$

Here, $\rho(t,\mathbf{x}) \geqslant 0$ represents the density, $p(t,\mathbf{x}) \in \mathbb{R}$ the pressure and $\mathbf{u}(t,\mathbf{x}) \in \mathbb{R}^2$ the velocity field of the fluid. The description of the external force is embodied into the right hand side $\mathbf{f}(t,\mathbf{x})$ of (3) and $\mu > 0$ stands for the (dynamic) viscosity. The unknowns depend on time $t \geqslant 0$ and position $\mathbf{x} \in \Omega \subset \mathbb{R}^2$. Given vector fields $\mathbf{u}$ and $\mathbf{v}$ we set $\mathrm{div}_{\mathbf{x}}(\mathbf{u}) = \sum_{i=1}^2 \partial_{x_i} u_i$, and $\mathbf{u} \otimes \mathbf{v}$ is the 2×2 matrix with components $u_i v_j$; given a matrix valued function A we denote $\mathrm{Div}_{\mathbf{x}} A$ the vector having components $\sum_{j=1}^2 \partial_{x_j} A_{ij}$.

There are several difficulties for solving numerically the system. To start with, the divergence free constraint and the underlying definition of the pressure have to be considered carefully. In particular, it yields some constraints between the spaces of approximation for the velocity and the pressure (the so–called "inf–sup condition") and many finite element methods have been designed for the treatment of the space homogeneous density incompressible Navier–Stokes equations. However, dealing with inhomogeneous densities leads to new numerical issues in order to treat the coupling with accuracy and the standard finite elements methods cannot be applied directly. The coupling also yields specific stability and conditioning questions. Classical illustrations consist in simulating the formation of Rayleigh–Taylor instabilities and the motion of

droplets or bubbles in a fluid. Clearly, increasing the ratio of the extreme densities – that can be associated to the so-called Atwood number – makes the problem more challenging for numerics. We refer for instance to [7,28,11] for a further description of these difficulties and discussion of techniques to treat the problem. In [11], we have introduced an original hybrid finite volume/finite element scheme to compute the solution of (2)–(4).

Let us denote Δt the time step and $t^n = n\Delta t$, $n \geqslant 0$. Let us assume that the numerical solution at time t^n, namely $(\rho^n, \mathbf{u}^n, p^n)$, is known on the computational domain. The numerical scheme is based on a time splitting of the system (2)–(4) known as the "Strang splitting" [42]:

1. An intermediate density field, $\rho^{n+\frac{1}{2}}$, is computed by solving on the time interval $(n\Delta t, (n+\frac{1}{2})\Delta t)$ the transport equation

$$\partial_t \rho^{n+\frac{1}{2}} + \mathrm{div}_{\mathbf{x}}(\rho^{n+\frac{1}{2}}\mathbf{u}^n) = 0, \tag{5}$$

with suitable boundary conditions on $\rho^{n+\frac{1}{2}}$, using a vertex-based finite volume method.
2. The new velocity and pressure fields, $\mathbf{u}^{n+1}$ and p^{n+1}, are computed by the resolution on the time interval $(n\Delta t, (n+1)\Delta t)$ of the system

$$\rho^{n+\frac{1}{2}}\left(\partial_t \mathbf{u}^{n+1} + \mathbf{u}^{n+1}\cdot\nabla_{\mathbf{x}}\mathbf{u}^{n+1}\right) + \nabla_{\mathbf{x}} p^{n+1} - \mu\Delta_{\mathbf{x}}\mathbf{u}^{n+1} = \mathbf{f}^{n+1}, \tag{6}$$

$$\mathrm{div}_{\mathbf{x}}\mathbf{u}^{n+1} = 0, \tag{7}$$

completed by the specification of boundary conditions on $\mathbf{u}^{n+1}$, using a finite element method.
3. Finally, the new density field, ρ^{n+1}, is computed by solving on the time interval $((n+\frac{1}{2})\Delta t, (n+1)\Delta t)$ the transport equation

$$\partial_t \rho^{n+1} + \mathrm{div}_{\mathbf{x}}(\rho^{n+1}\mathbf{u}^{n+1}) = 0, \tag{8}$$

with suitable boundary conditions on ρ^{n+1}, using once again the vertex-based finite volume method.

Then we go back to the first step (using $n+1$ instead of n) to compute the solution at the following time step. A key point of the method introduced in [11] is the "compatibility relation", which has to be carefully fulfilled so that the discrete divergence free constraint is ensured both for the finite element and the finite volume interpretations. We will not come back on this point here neither on the description of the global numerical scheme. We only consider that we have to solve (5) and (8), having at hand a given discrete velocity field $\mathbf{u}$. In particular, in view of the application we have in mind, it turns out that

- it is natural to keep track of the interfaces and to appeal to mesh refinements strategies so that a fine grid is used only in regions of steep density gradients and a coarse grid elsewhere.
- as the density ratio increases (considering air and water this ratio is of order of 1000) the simulation becomes highly sensitive to violation of the maximum principle which might lead to severe numerical instabilities for the whole system.

2.2. Space discretization and notations

Let $\partial\Omega$ be the Lipschitz boundary of Ω, and $\mathbf{n}(\mathbf{x})$ the outer unit normal vector at $\mathbf{x} \in \partial\Omega$. Let $\mathcal{T}_h$ be a partition of Ω (named primal mesh) composed of conforming and isotropic triangles T_k, with $k \in [1,K]$. For each element T_k of the mesh, we denote B_k the barycenter of the triangle and $|T_k|$ the area of T_k. Moreover, we denote by A_i, $i \in [1,I]$, the vertices of $\mathcal{T}_h$. For a given node A_i, let $\mathcal{V}(i)$ be the set of the indices of the neighboring nodes A_j which are vertices of the elements T_k sharing the common point A_i. For a given triangle T_i, let $\mathcal{W}(i)$ be the set of the indices of the neighboring triangles T_j sharing at least one node with T_i. We also denote by A_{ij} the middle point of the edge $[A_iA_j]$. For each vertex A_i, we associate a polygon denoted by $\mathcal{C}_i$, which defines a second partition of Ω (named dual mesh). Here, this polygon $\mathcal{C}_i$ is defined by joining the barycenters B_k of the neighboring elements T_k which share the node A_i with the middle points A_{ij} of the edges $[A_iA_j]$, for $j \in \mathcal{V}(i)$. This construction is referred to as the "CV1" control volume (see Fig. 1), and we will see later that a variant can be proposed. We denote Γ_{ij}^- (resp. Γ_{ij}^+) the segment $[B_{j-1}A_{ij}]$ (resp. $[A_{ij}B_j]$) (here we visit the neighboring triangles around A_i in the counterclockwise direction), A_{ij}^- (resp. A_{ij}^+) the middle of Γ_{ij}^- (resp. Γ_{ij}^+) and $\mathbf{n}_{ij}^-$ (resp. $\mathbf{n}_{ij}^+$) the unit outward normal to $\mathcal{C}_i$ along Γ_{ij}^- (resp. Γ_{ij}^+). Let $|\mathcal{C}_i|$ stand for the area of $\mathcal{C}_i$ and $|\Gamma_{ij}^-|$ (resp. $|\Gamma_{ij}^+|$) for the length of Γ_{ij}^- (resp. Γ_{ij}^+). Then, the boundary of $\mathcal{C}_i$ splits into several segments Γ_{ij}^- and Γ_{ij}^+ and we write $\partial\mathcal{C}_i = \bigcup_{j\in\mathcal{V}(i)}(\Gamma_{ij}^- \cup \Gamma_{ij}^+)$.

We introduce now the following quantity

$$C_{\mathcal{T}_h} = \max_{T_j\in\mathcal{T}_h}\max_{k\in\mathcal{W}(j)}\frac{d_{T_j}}{h_{T_k}}, \tag{9}$$

where d_{T_j} is the diameter of the circumscribed circle to T_j and h_{T_k} the smallest height in T_k. The constant $C_{\mathcal{T}_h}$ measures the mesh size variation from an element to a neighboring one and characterizes the mesh regularity. Let us note that it does not exactly correspond to the usual elementwise aspect ratio in the Ciarlet sense [14], but it is of the same order for usual isotropic meshes like those used in this paper. The constant $C_{\mathcal{T}_h}$ is clearly bounded from below by 1; the smaller the value of

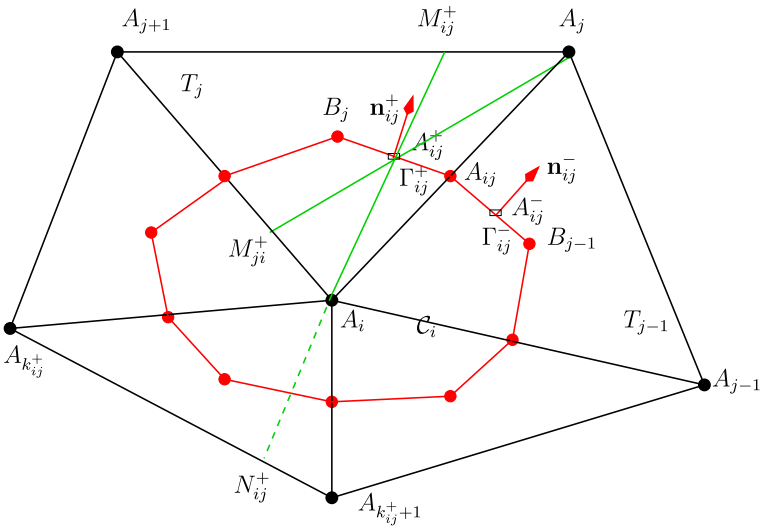

Fig. 1. Construction of the dual mesh: control volume CV1 around the node A_i.

$C_{\mathcal{T}_h}$, the more regular the mesh. For example, the particular mesh in Fig. 2 verifies $C_{\mathcal{T}_h} = 2$. In practice, standard isotropic mesh generators provide meshes with controlled values of this parameter.

2.3. Finite volume scheme

As said above, let us assume that ρ^n, the numerical solution at time t^n, is known on the computational domain. The new density ρ^{n+1} is computed by solving on the time interval $(n\Delta t,(n+1)\Delta t)$ the transport equation

$$\partial_t \rho^{n+1} + \mathrm{div}_{\mathbf{x}}(\rho^{n+1}\mathbf{u}) = 0. \tag{10}$$

Here and below, the velocity field is a given function $\mathbf{u} : \mathbb{R} \times \mathbb{R}^2 \to \mathbb{R}^2$ which fulfills the divergence free condition. We will make more precise this requirement at the discrete level later on. The computation of the solution is performed using a usual vertex-based finite volume (FV) scheme which provides the approximated value $\rho_i^{n+1},\ i \in [1,I]$:

$$\rho_i^{n+1} \approx \frac{1}{|\mathcal{C}_i|}\int_{\mathcal{C}_i} \rho(t^{n+1},\mathbf{x})\mathrm{d}\mathbf{x}.$$

Let us remark that the vertex-based choice of the FV method (instead of the cell-centered one) allows to write a $\mathbb{P}_1$ Lagrange interpolation of the density if needed, by using this constant value ρ_i^{n+1} on $\mathcal{C}_i$ as the value of ρ^{n+1} at node A_i (see [11]). Then, $\rho_i^{n+1},\ i \in [1,I]$ is computed by using the formula

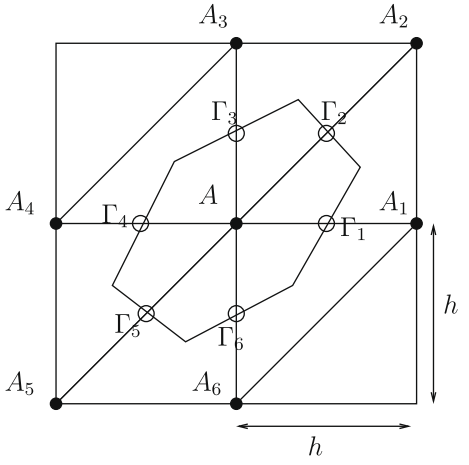

Fig. 2. A particular mesh.

$$\rho_i^{n+1} = \rho_i^n - \frac{\Delta t}{|\mathcal{C}_i|} \sum_{j\in\mathcal{V}(i)} \Big(|\Gamma_{ij}^+| G_{ij}^+((\rho_{ij}^+)^n, (\rho_{ji}^+)^n) + |\Gamma_{ij}^-| G_{ij}^-((\rho_{ij}^-)^n, (\rho_{ji}^-)^n) \Big), \tag{11}$$

where the right hand side of (11) is evaluated using an upstream flux:

$$G_{ij}^{\pm}(\rho_1,\rho_2) = \begin{cases} \rho_1 \mathbf{u}_{ij}^{\pm}\cdot\mathbf{n}_{ij}^{\pm} & \text{if } \mathbf{u}_{ij}^{\pm}\cdot\mathbf{n}_{ij}^{\pm} \geqslant 0, \\ \rho_2 \mathbf{u}_{ij}^{\pm}\cdot\mathbf{n}_{ij}^{\pm} & \text{if } \mathbf{u}_{ij}^{\pm}\cdot\mathbf{n}_{ij}^{\pm} < 0. \end{cases} \tag{12}$$

This is a natural choice having in mind a further MUSCL treatment to reach higher accuracy. With this choice, the monotone property of the numerical flux is ensured, namely:

$$\frac{\partial G_{ij}^{\pm}}{\partial \rho_1}(\rho_1,\rho_2) \geqslant 0 \quad \text{and} \quad \frac{\partial G_{ij}^{\pm}}{\partial \rho_2}(\rho_1,\rho_2) \leqslant 0. \tag{13}$$

In (12), $\mathbf{u}_{ij}^+$ (resp. $\mathbf{u}_{ij}^-$) stands for the value of the velocity field at the point A_{ij}^+ (resp. A_{ij}^-). In fact, bearing in mind multiphysics coupled models, the velocity field is also known on a discrete way, and $\mathbf{u}_{ij}^+$ is rather an approximation of the continuous velocity associated to the point A_{ij}^+. (Coming back to [11], it is defined from the finite element discretization of the momentum equation of the Navier–Stokes system.) Therefore, the discrete velocity field is defined so that it preserves the continuous divergence free property at the discrete level: for any given constant density ρ_c on the whole domain, and whatever $i \in [1,I]$,

$$\sum_{j\in\mathcal{V}(i)} \Big(|\Gamma_{ij}^+| G_{ij}^+(\rho_c,\rho_c) + |\Gamma_{ij}^-| G_{ij}^-(\rho_c,\rho_c) \Big) = 0 \tag{14}$$

holds. The consistency property (14) is a key point of the further analysis. A first order accuracy in space is obtained by choosing, as interface reconstruction involved in (11), the value $(\rho_{ij}^+)^n = (\rho_{ij}^-)^n = \rho_i^n$ for all $i \in [1,I]$ and $j \in \mathcal{V}(i)$. It is well-established that in this case the L^∞ stability is satisfied under an appropriate CFL condition. The second-order accuracy in space can be reached by using a MUSCL technique [44,45], with a reconstruction operator which gives new values $\rho_{ij}^{\pm}$ and $\rho_{ji}^{\pm}$ on both sides of $\Gamma_{ij}^{\pm}$ using the values ρ_i^n, ρ_j^n and ρ_k^n for some $k \in \mathcal{V}(i)\cup\mathcal{V}(j)$. In this work, we aim at developing such a reconstruction strategy with the goal of preserving the local maximum property:

$$\forall i \in [1,I], \quad \min_{j\in\mathcal{V}(i)}(\rho_i^n,\rho_j^n) \leqslant \rho_i^{n+1} \leqslant \max_{j\in\mathcal{V}(i)}(\rho_i^n,\rho_j^n), \tag{15}$$

in a vertex-based finite-volume context. For further considerations it is convenient to introduce the quantity:

$$\|\mathbf{u}\|_{i,\infty} = \max_{j\in\mathcal{V}(i)} \max(\|\mathbf{u}_{ij}^+\|_{l^2(\mathbb{R}^2)}, \|\mathbf{u}_{ij}^-\|_{l^2(\mathbb{R}^2)}). \tag{16}$$

2.4. Second-order reconstruction

2.4.1. Monoslope procedure

A classical approach to reach the second-order accuracy is based on a piecewise linear approximation of the density defined using a gradient vector of the unknown. The upstream or downstream gradient vectors can so be defined on each element T_k or on each node A_i of $\mathcal{T}_h$. Usually, $(\nabla\rho)_{|_{T_k}}$, $k \in [1,K]$, is the gradient vector computed from the three values of ρ^n in the triangle T_k, $\nabla\rho_i = (\sum_{k\in\mathcal{Z}(i)}|T_k|(\nabla\rho)_{|_{T_k}})/(\sum_{k\in\mathcal{Z}(i)}|T_k|), i \in [1,I]$, with $\mathcal{Z}(i)$ the set of the indices of the triangles T_k sharing A_i [25,8]. Using this approach on unstructured meshes, by considering a one-dimensional problem independently for each interface reconstruction, it is easy to see that the maximum principle will not be respected. To illustrate it, let us consider the following example where a density field is defined on the mesh given in Fig. 2: ρ^n is the density value at node A and ρ_i^n at node A_i, $1 \leqslant i \leqslant 6$ (see full circles). The density is identically equal to 1 ($\rho^n = \rho_2^n = \rho_3^n = \rho_4^n = \rho_5^n = \rho_6^n = 1$), except at node A_1 where $\rho_1^n = 1+\varepsilon$, $\varepsilon > 0$. We are interested in the new value of the density at node A after one iteration in time, namely ρ^{n+1}, using (41) (see below) which is a variant of (11) in the particular case of such a structured mesh. The velocity $\mathbf{u}$ is supposed to be equal to $\mathbf{u} = (1,0)^T$. We use the one-dimensional reconstruction with the β-scheme, $\beta = \frac{1}{3}$, and the Van-Leer limiter. Thus it is necessary to reconstruct the value of the density on each part of the interface of the control volume (see empty circles). Using one of the usual way to proceed [8], the reconstructed value $\tilde{\rho}_1^n$ of the density at interface Γ_1 located between A and A_1 is computed by:

$$\tilde{\rho}_1^n = \rho^n + \frac{1}{2}\Big[\beta\alpha(r_1)\overline{\Delta\rho}_1 + (1-\alpha(r_1))(1-\beta)\underline{\Delta\rho}_1\Big],$$

where $\beta = \frac{1}{3}$, $r_1 = \frac{\beta\overline{\Delta\rho}_1}{(1-\beta)\underline{\Delta\rho}_1}$, α is the Van-Leer flux-limiter function $\left(\alpha(r) = \frac{r+|r|}{1+r}\right)$, $\overline{\Delta\rho}_1$ is the "upstream" variation of the density, computed here using an averaged value of the density gradients in triangles surrounding the node A, and $\underline{\Delta\rho}_1$ is the "downstream" variation of the density, computed with the values of the density only at nodes A and A_1. Using such a strategy, we naturally arrive at:

$$\tilde{\rho}_1^n = 1 + \frac{16}{63}\varepsilon; \quad \tilde{\rho}_2^n = \tilde{\rho}_3^n = \tilde{\rho}_4^n = \tilde{\rho}_5^n = \tilde{\rho}_6^n = 1.$$

Consequently, a simple calculation using (41) and geometrical considerations of this particular control volume lead to:

$$\frac{h^2}{\Delta t}(\rho^{n+1} - \rho^n) = -\frac{32h}{189}\varepsilon < 0,$$

and neither the maximum principle nor the local extremum diminishing (LED) properties of the scheme are fulfilled since $\rho^{n+1} < 1$. Such an approach can nevertheless ensure the maximum principle property in particular cases corresponding to Cartesian meshes on which a tensorial analysis can be performed, coming back under a given CFL to the one-dimensional framework.

A first remedy is so to consider a monoslope method, as introduced in [30,9] for the cell-centered framework. The idea of [30] can be adapted to the vertex-based context. It would consist in the computation of a gradient operator, the vector $\nabla\rho_i$ for example, and to use only this gradient on the volume $\mathcal{C}_i$ in order to obtain all the reconstructed values $(\rho_{ij}^+)^n$ (resp. $(\rho_{ij}^-)^n$) on the segments Γ_{ij}^+ (resp. Γ_{ij}^-), $j \in \mathcal{V}(i)$. A limiting strategy would then be applied in order to avoid the creation of new extrema during the reconstruction process: it is indeed in this approach a necessary condition to ensure the maximum principle property (see the appendix of [6] for the proof). So we would have:

$$\rho_{ij}^{\pm} = \rho_i + \alpha_i \nabla\rho_i \cdot \mathbf{A_i A_{ij}^{\pm}} \text{ for any } j \in \mathcal{V}(i),$$

where $\alpha_i \in [0,1]$ has to be determined not to create any new extremum at the interface. Hence, the limiting procedure can reduce drastically the scheme locally to the order one in all the space directions around A_i, while it is only needed for one of these directions. It constitutes a severe drawback, even for very regular solutions. Nevertheless, if this methodology is used, a sufficient condition to obtain the maximum principle remains that the linear approximation satisfies the following conservation property:

$$\int_{\mathcal{C}_i} (\rho_i + \alpha_i \nabla\rho_i \cdot \mathbf{A_i X}) d\mathbf{X} = |\mathcal{C}_i|\rho_i \quad \forall i \in [1, I].$$

It can be immediately seen that if a cell-centered FV approach automatically satisfies the conservation property, because of the triangular geometry of the control volume, it is not the case with the vertex-based FV approach for which the control volume is a given polygonal. This is the reason why a multislope multi-dimensional procedure is necessary in the vertex-based context, as confirmed by numerical experiments.

2.4.2. Multislope procedure

We need to introduce a few notation, see Fig. 1. Given two points D and E in the plane, we denote (DE) the line passing through D and E, and $(DE[$ is the half-line starting from E and containing D (but not E). Moreover, we define $\mathcal{D}_i = \cup_{A_i \in T_k} T_k$. Obviously, $\mathcal{C}_i \subset \mathcal{D}_i$. This subsection is devoted to the description of the density reconstruction $(\rho_{ij}^+)^n$ on the interface Γ_{ij}^+ by a multislope strategy. Of course, a similar reconstruction will be derived for the value of $(\rho_{ij}^-)^n$, as well as for the values of $(\rho_{ji}^+)^n$ and $(\rho_{ji}^-)^n$. In order to simplify the notations, the time indices are dropped; ρ_{ij}^+ will so have to be understood as $(\rho_{ij}^+)^n$. Finally, the node A_i is supposed not to belong to the boundary of Ω (in other words, it is an internal node). We introduce the point $M_{ij}^+ = (A_iA_{ij}^+) \cap [A_jA_{j+1}]$.

Definition 1. Let us define $\alpha_{i,j}^+ \in [0,1]$ such that:

$$\mathbf{A_i M_{ij}^+} = \alpha_{i,j}^+ \mathbf{A_i A_j} + (1 - \alpha_{i,j}^+)\mathbf{A_i A_{j+1}} \tag{17}$$

This definition, associated to a $\mathbb{P}_1$-Lagrange-piecewise interpretation of the density field on the primal mesh, allows to define a density value at nodes M_{ij}^+ by setting:

$$\rho_{M_{ij}^+} = \rho_i + \alpha_{i,j}^+(\rho_j - \rho_i) + (1 - \alpha_{i,j}^+)(\rho_{j+1} - \rho_i).$$

Now, we define the point $N_{ij}^+ = (A_iM_{ij}^+[\cap \partial\mathcal{D}_i$.

Definition 2. Let us introduce $k_{ij}^+ \in \mathcal{V}(i)$ and $\alpha_{i,k_{ij}^+} \in [0,1]$ such that:

$$\mathbf{A_i N_{ij}^+} = \alpha_{i,k_{ij}^+} \mathbf{A_i A_{k_{ij}^+}} + (1 - \alpha_{i,k_{ij}^+})\mathbf{A_i A_{k_{ij}^+ + 1}} \tag{18}$$

Once again, this definition allows to define a density value at nodes N_{ij}^+ by setting:

$$\rho_{N_{ij}^+} = \rho_i + \alpha_{i,k_{ij}^+}(\rho_{k_{ij}^+} - \rho_i) + (1 - \alpha_{i,k_{ij}^+})(\rho_{k_{ij}^+ + 1} - \rho_i). \tag{19}$$

To define the interface reconstruction ρ_{ij}^+ involved in (11), we first set

$$p_{ij}^{up} = \frac{\rho_i - \rho_{N_{ij}^+}}{\|\mathbf{A}_i\mathbf{N}_{ij}^+\|}, \quad p_{ij}^{down} = \frac{\rho_{M_{ij}^+} - \rho_i}{\|\mathbf{A}_i\mathbf{M}_{ij}^+\|},$$
$$r_{ij} = \frac{p_{ij}^{down}}{p_{ij}^{up}}, \qquad p_{ij} = p_{ij}^{up}\Psi(r_{ij}),$$

where Ψ is the flux limiter function, which is assumed to satisfy:

$$\begin{cases} \Psi(r) = 0 & \text{if } r \leqslant 0; \\ \Psi(r) > 0 & \text{if } r > 0. \end{cases} \tag{20}$$

Let us note that to reach second-order accuracy and to preserve a linear solution, we have also to impose $\Psi(1) = 1$ (see Sweby's diagram in [31]). Then, ρ_{ij}^+ is finally defined as:

$$\rho_{ij}^+ = \rho_i + p_{ij}\|\mathbf{A}_i\mathbf{A}_{ij}^+\|. \tag{21}$$

3. Local maximum principle property

3.1. Preliminary results

Definition 3 (*Convexity property*). The second-order reconstruction ρ_{ij}^+ is said to be convex if there exists $\theta_{ij}^+ \in [0,1]$ such that

$$\rho_{ij}^+ = (1 - \theta_{ij}^+)\rho_i + \theta_{ij}^+\rho_{M_{ij}^+}. \tag{22}$$

Definition 4 (τ-*limiter*). Let $\tau > 0$; Ψ is said to be a τ-limiter if it satisfies the property:

$$\forall r \in \mathbb{R}_*^+, \quad \Psi(r) \leqslant \min\left(\frac{12}{7}r, \tau\right) \tag{23}$$

Remark 1. This definition slightly differs from the "Q-limiter" property arising in the cell-centered context [16]. For example, instead of 12/7, a coefficient depending on the mesh regularity has to be introduced. Remark that the *minmod* limiter is a τ-limiter with $\tau = 1$, and that several other less-diffusive usual one-dimensional limiters can be adapted to easily become τ-limiters. For example, with $\tau = 12/7$, the modified superbee limiter is

$$\Psi(r) = \max(0, \min(1, \tau r), \min(r, \tau)),$$

instead of the classical one, defined similarly by using $\tau = 2$. Again with $\tau = 12/7$, the modified Van-Leer limiter is (see [31] and [16, p. 81])

$$\Psi(r) = \begin{cases} 0 & \text{if} r \leqslant 0; \\ \frac{r+(\tau-1)r}{1+(\tau-1)r} & \text{if } 0 \leqslant r \leqslant 1; \\ \frac{r+(\tau-1)r}{(\tau-1)+r} & \text{if } r \geqslant 1. \end{cases} \tag{24}$$

Of course, these modified limiters lie in Sweby's region.

Lemma 1. *If Ψ is a τ-limiter, then the reconstruction (21) is a convex reconstruction.*

Proof 1. The proof is very similar to the one developed in [16] in the cell-centered context. Without loss of generality, let suppose that $\rho_i \leqslant \rho_{M_{ij}^+}$, so that $p_{ij}^{down} \geqslant 0$. If $p_{ij}^{up} < 0$, then the scheme degenerates to order 1 and (22) is obviously fulfilled with $\theta_{ij}^+ = 0$. If $p_{ij}^{up} \geqslant 0$, (21) ensures that $\rho_{ij}^+ \geqslant \rho_i$. On the other hand, since from geometrical considerations $\mathbf{A}_i\mathbf{A}_{ij}^+ = \frac{7}{12}\mathbf{A}_i\mathbf{M}_{ij}^+$ and using the fact that Ψ is a τ-limiter, we get:

$$p_{ij} \leqslant \frac{\|\mathbf{A}_i\mathbf{M}_{ij}^+\|}{\|\mathbf{A}_i\mathbf{A}_{ij}^+\|}p_{ij}^{down},$$

leading directly to $\rho_{ij}^+ \leqslant \rho_{M_{ij}^+}$. □

Lemma 2. *There exists some coefficients $w_{ijk}^+ \geqslant 0$, $k \in \mathcal{V}(i)$, such that*

$$\rho_{ij}^+ - \rho_i = \sum_{k\in\mathcal{V}(i)} w_{ijk}^+(\rho_i - \rho_k) \tag{25}$$

holds, and furthermore, they satisfy

$$\sum_{k\in\mathcal{V}(i)} w_{ijk}^{+} \leqslant \frac{7\tau}{12} C_{\mathcal{T}_h}. \tag{26}$$

Remark 2. This result is an adaptation of the so-called "Chainais–Hillairet condition", see [12], developed in the cell-centered approach. But in the cell-centered framework, it relies on additional geometrical assumptions on the mesh. Adopting a vertex-based viewpoint relaxes the geometrical constraints needed to prove such a statement.

Proof 2. Let us define:

$$\Delta\rho_{ij}^{+} = \rho_{ij}^{+} - \rho_i = p_{ij}\|\mathbf{A}_i\mathbf{A}_{ij}^{+}\|.$$

If $p_{ij}^{down}p_{ij}^{up} \leqslant 0$, then $\Delta\rho_{ij}^{+} = 0$ and we can set $w_{ijk}^{+} = 0$. Let us discuss the case $p_{ij}^{down}p_{ij}^{up} > 0$. By (19), we get:

$$\Delta\rho_{ij}^{+} = [\alpha_{i,k_{ij}^{+}}(\rho_i - \rho_{k_{ij}^{+}}) + (1-\alpha_{i,k_{ij}^{+}})(\rho_i - \rho_{k_{ij}^{+}+1})]\Psi(r_{ij})\frac{\|\mathbf{A}_i\mathbf{A}_{ij}^{+}\|}{\|\mathbf{A}_i\mathbf{N}_{ij}^{+}\|}.$$

By a simple identification, the coefficients w_{ijk}^{+} can obviously be derived to fulfill (25): we set

$$w_{ijk}^{+} = \begin{cases} \alpha_{i,k_{ij}^{+}}\Psi(r_{ij})\frac{\|\mathbf{A}_i\mathbf{A}_{ij}^{+}\|}{\|\mathbf{A}_i\mathbf{N}_{ij}^{+}\|} & \text{if } k = k_{ij}^{+}, \\ (1-\alpha_{i,k_{ij}^{+}})\Psi(r_{ij})\frac{\|\mathbf{A}_i\mathbf{A}_{ij}^{+}\|}{\|\mathbf{A}_i\mathbf{N}_{ij}^{+}\|} & \text{if } k = k_{ij}^{+}+1, \\ 0 & \text{in any other case.} \end{cases}$$

Now, in order to prove (26), we have to write

$$\sum_{k\in\mathcal{V}(i)} w_{ijk}^{+} = \Psi(r_{ij})\frac{\|\mathbf{A}_i\mathbf{A}_{ij}^{+}\|}{\|\mathbf{A}_i N_{ij}^{+}\|} = \Psi(r_{ij})\frac{\|\mathbf{A}_i\mathbf{A}_{ij}^{+}\|}{\|\mathbf{A}_i\mathbf{M}_{ij}^{+}\|}\frac{\|\mathbf{A}_i\mathbf{M}_{ij}^{+}\|}{\|\mathbf{A}_i\mathbf{N}_{ij}^{+}\|} \leqslant \frac{7\tau}{12}C_{\mathcal{T}_h}$$

because of (23) and (9). □

3.2. L^∞ stability

Theorem 1. *Let Ψ be a τ-limiter. The numerical scheme (11) associated to the numerical flux (12) and the second-order reconstruction at the interfaces described in Section 2.4.2 respects the local maximum principle under the CFL condition:*

$$\Delta t \leqslant \min_{1\leqslant i\leqslant I} \frac{|\mathcal{C}_i|}{\|\mathbf{u}\|_{i,\infty}\left(2+\frac{7\tau}{12}C_{\mathcal{T}_h}\right)\sum_{j\in\mathcal{V}(i)}(|\Gamma_{ij}^{+}| + |\Gamma_{ij}^{-}|)}. \tag{27}$$

Proof 3. Making use of the consistency property (14), the numerical scheme (11) can be written as follows (remind that the indices n are dropped in the right-hand side)

$$\begin{aligned} \rho_i^{n+1} &= \rho_i - \frac{\Delta t}{|\mathcal{C}_i|}\sum_{j\in\mathcal{V}(i)}|\Gamma_{ij}^{+}|\left(G_{ij}^{+}(\rho_{ij}^{+},\rho_{ji}^{+}) - G_{ij}^{+}(\rho_i,\rho_i)\right) - \frac{\Delta t}{|\mathcal{C}_i|}\sum_{j\in\mathcal{V}(i)}|\Gamma_{ij}^{-}|\left(G_{ij}^{-}(\rho_{ij}^{-},\rho_{ji}^{-}) - G_{ij}^{-}(\rho_i,\rho_i)\right) \\ &= \rho_i - \frac{\Delta t}{|\mathcal{C}_i|}\sum_{j\in\mathcal{V}(i)}|\Gamma_{ij}^{+}|\left(G_{ij}^{+}(\rho_i+\Delta\rho_{ij}^{+},\rho_i+\tilde{\Delta}\rho_{ij}^{+}) - G_{ij}^{+}(\rho_i,\rho_i)\right) \\ &\quad - \frac{\Delta t}{|\mathcal{C}_i|}\sum_{j\in\mathcal{V}(i)}|\Gamma_{ij}^{-}|\left(G_{ij}^{-}(\rho_i+\Delta\rho_{ij}^{-},\rho_i+\tilde{\Delta}\rho_{ij}^{-}) - G_{ij}^{-}(\rho_i,\rho_i)\right), \end{aligned} \tag{28}$$

where we defined:

$$\begin{aligned} \Delta\rho_{ij}^{+} &= \rho_{ij}^{+} - \rho_i, \quad \tilde{\Delta}\rho_{ij}^{+} = \rho_{ji}^{+} - \rho_i, \\ \Delta\rho_{ij}^{-} &= \rho_{ij}^{-} - \rho_i, \quad \tilde{\Delta}\rho_{ij}^{-} = \rho_{ji}^{-} - \rho_i. \end{aligned}$$

Now, by considering the functions $h^{\pm} : \theta \in [0,1] \to h^{\pm}(\theta) = G_{ij}^{\pm}(\rho_i + \theta\Delta\rho_{ij}^{\pm}, \rho_i + \theta\tilde{\Delta}\rho_{ij}^{\pm})$, and by using the finite variations theorem, we get the existence of $0 < \zeta_{ij}^{\pm} < 1$ such that:

$$\rho_i^{n+1} = \rho_i - \Delta t\sum_{j\in\mathcal{V}(i)}(A_{ij}^{+}\Delta\rho_{ij}^{+} - B_{ij}^{+}\tilde{\Delta}\rho_{ij}^{+}) - \Delta t\sum_{j\in\mathcal{V}(i)}(A_{ij}^{-}\Delta\rho_{ij}^{-} - B_{ij}^{-}\tilde{\Delta}\rho_{ij}^{-}), \tag{29}$$

where we introduced (see (12) and (13))

$$A_{ij}^{\pm} = \frac{|\Gamma_{ij}^{\pm}|}{|\mathcal{C}_i|}\frac{\partial G_{ij}^{\pm}}{\partial \rho_1}(\rho_i + \zeta_{ij}^{\pm}\Delta\rho_{ij}^{\pm}, \rho_i + \zeta_{ij}^{\pm}\tilde{\Delta}\rho_{ij}^{\pm}),$$
$$B_{ij}^{\pm} = -\frac{|\Gamma_{ij}^{\pm}|}{|\mathcal{C}_i|}\frac{\partial G_{ij}^{\pm}}{\partial \rho_2}(\rho_i + \zeta_{ij}^{\pm}\Delta\rho_{ij}^{\pm}, \rho_i + \zeta_{ij}^{\pm}\tilde{\Delta}\rho_{ij}^{\pm}).$$

Because of the definition of the monotone property of the flux (13), we clearly have $A_{ij}^{\pm} \geqslant 0$ and $B_{ij}^{\pm} \geqslant 0$. On the one hand, Lemma 2 allows to write:

$$\Delta\rho_{ij}^{+} = \sum_{k\in\mathcal{V}(i)} w_{ijk}^{+}(\rho_i - \rho_k) \text{ with } w_{ijk}^{+} \geqslant 0 \quad \text{and} \quad \sum_{k\in\mathcal{V}(i)} w_{ijk}^{+} \leqslant \frac{7\tau}{12}C_{\mathcal{T}_h},$$

and similarly:

$$\Delta\rho_{ij}^{-} = \sum_{k\in\mathcal{V}(i)} w_{ijk}^{-}(\rho_i - \rho_k) \text{ with } w_{ijk}^{-} \geqslant 0 \quad \text{and} \quad \sum_{k\in\mathcal{V}(i)} w_{ijk}^{-} \leqslant \frac{7\tau}{12}C_{\mathcal{T}_h}.$$

On the other hand, thanks to Lemma 1, the convex property of the reconstruction leads to:

$$\tilde{\Delta}\rho_{ij}^{+} = \theta_{ji}^{+}(\rho_{M_{ji}^{+}} - \rho_j) + (\rho_j - \rho_i) = \theta_{ji}^{+}(\rho_{M_{ji}^{+}} - \rho_i) + (1 - \theta_{ji}^{+})(\rho_j - \rho_i).$$

Since $M_{ji}^{+} \in [A_iA_{j+1}]$, $\rho_{M_{ji}^{+}}$ is defined by a linear interpolation between ρ_i and ρ_{j+1}. So we get:

$$\tilde{\Delta}\rho_{ij}^{+} = \theta_{ji}^{+}\frac{\|\mathbf{A}_i\mathbf{M}_{ji}^{+}\|}{\|\mathbf{A}_i\mathbf{A}_{j+1}\|}(\rho_{j+1} - \rho_i) + (1 - \theta_{ji}^{+})(\rho_j - \rho_i). \tag{30}$$

By identification, we can find some coefficients $\tilde{w}_{ijk}^{+}$ such that:

$$\tilde{\Delta}\rho_{ij}^{+} = \sum_{k\in\mathcal{V}(i)} \tilde{w}_{ijk}^{+}(\rho_k - \rho_i) \text{ with } \tilde{w}_{ijk}^{+} \geqslant 0 \quad \text{and} \quad \sum_{k\in\mathcal{V}(i)} \tilde{w}_{ijk}^{+} \leqslant 2.$$

Similarly, we find $\tilde{w}_{ijk}^{-}$ satisfying

$$\tilde{\Delta}\rho_{ij}^{-} = \sum_{k\in\mathcal{V}(i)} \tilde{w}_{ijk}^{-}(\rho_k - \rho_i) \text{ with } \tilde{w}_{ijk}^{-} \geqslant 0 \quad \text{and} \quad \sum_{k\in\mathcal{V}(i)} \tilde{w}_{ijk}^{-} \leqslant 2.$$

The numerical scheme (29) can now be recast as follows

$$\rho_i^{n+1} = \rho_i - \Delta t \sum_{k,j\in\mathcal{V}(i)} (A_{ij}^{+}w_{ijk}^{+}(\rho_i - \rho_k) - B_{ij}^{+}\tilde{w}_{ijk}^{+}(\rho_k - \rho_i)) - \Delta t \sum_{k,j\in\mathcal{V}(i)} (A_{ij}^{-}w_{ijk}^{-}(\rho_i - \rho_k) - B_{ij}^{-}\tilde{w}_{ijk}^{-}(\rho_k - \rho_i)), \tag{31}$$

which can be written as:

$$\rho_i^{n+1} = c_{ii}\rho_i + \sum_{k\in\mathcal{V}(i)} c_{ik}\rho_k, \tag{32}$$

with:

$$\begin{cases} c_{ii} = 1 - \Delta t \sum\limits_{k,j\in\mathcal{V}(i)} \left(A_{ij}^{+}w_{ijk}^{+} + B_{ij}^{+}\tilde{w}_{ijk}^{+} + A_{ij}^{-}w_{ijk}^{-} + B_{ij}^{-}\tilde{w}_{ijk}^{-}\right), \\ c_{ik} = \Delta t \sum\limits_{j\in\mathcal{V}(i)} \left(A_{ij}^{+}w_{ijk}^{+} + B_{ij}^{+}\tilde{w}_{ijk}^{+} + A_{ij}^{-}w_{ijk}^{-} + B_{ij}^{-}\tilde{w}_{ijk}^{-}\right). \end{cases}$$

We obviously have

$$c_{ii} + \sum_{k\in\mathcal{V}(i)} c_{ik} = 1. \tag{33}$$

Moreover, if Δt is now chosen such that whatever $i \in [1, I]$,

$$\Delta t \leqslant \left(\sum_{k,j\in\mathcal{V}(i)} \left(A_{ij}^{+}w_{ijk}^{+} + B_{ij}^{+}\tilde{w}_{ijk}^{+} + A_{ij}^{-}w_{ijk}^{-} + B_{ij}^{-}\tilde{w}_{ijk}^{-}\right)\right)^{-1}, \tag{34}$$

then we get:

$$0 \leqslant c_{ii} \leqslant 1 \quad \text{and} \quad 0 \leqslant c_{ik} \leqslant 1. \tag{35}$$

The scheme formulation (32) together with relations (33) and (35) on the coefficients leads to the local maximum preserving property, since ρ_i^{n+1} is written as a convex combination of ρ_i and ρ_j, $j \in \mathcal{V}(i)$. Now, in order to recover (27), we just have to

combine the fact that $A_{ij}^{\pm} \leqslant \frac{|\Gamma_{ij}^{\pm}|}{|\mathcal{C}_i|}\|\mathbf{u}\|_{i,\infty}$ and $B_{ij}^{\pm} \leqslant \frac{|\Gamma_{ij}^{\pm}|}{|\mathcal{C}_i|}\|\mathbf{u}\|_{i,\infty}$, associated to previous properties on the coefficients $w_{ijk}^{\pm}$ and $\tilde{w}_{ijk}^{\pm}$. □

Remark 3. In the particular case of a constant velocity $\mathbf{u}$ associated to a uniform mesh like the one in Fig. 2 with hexagonal control volumes ($C_{\mathcal{T}_h} = 2$) and with the use of the *minmod* limiter ($\tau = 1$), the CFL condition (27) leads to:

$$\Delta t \leqslant \frac{9h}{19(\sqrt{2}+2\sqrt{5})\|\mathbf{u}\|} \approx \frac{h}{12.4\|\mathbf{u}\|} \tag{36}$$

At first sight, (36) can appear as a very severe CFL restriction, but it is very similar to other CFL-conditions on unstructured meshes used to ensure the maximum principle, see for instance [22,13]. Moreover, we must bear in mind that all the proofs were established by considering sufficient conditions which always correspond to the worst case we could encounter. Consequently, it is observed in numerical computations that very good results are obtained even with less restrictive CFL numbers.

3.3. A variant of the numerical scheme

Instead of considering the dual mesh made of CV1 control volumes displayed in Fig. 1, we could build another dual mesh using more simple ones, by joining the barycenters of all the triangles surrounding A_i leading to "CV2" control volumes (see Fig. 3). In that case, we define $\Gamma_{ij} = [B_{j-1}B_j]$ as the interface between the nodes A_i and A_j, and we so have to reconstruct the density value at the node $Q_{ij} = [B_{j-1}B_j] \cap [A_iA_j]$. In general, Q_{ij} is no more the middle of $[A_iA_j]$, except in the case of very particular structured meshes. There are clearly several advantages with this construction. In particular, the downstream slope p_{ij}^{down} is now directly available without any linear interpolation process:

$$p_{ij}^{down} = \frac{\rho_j - \rho_i}{\|\mathbf{A_iA_j}\|},$$

even if the upstream gradient definition p_{ij}^{up} always needs the value of the density at node $N_{ij} = (A_iA_j[\cap\partial\mathcal{D}_i$ by a linear interpolation reconstruction:

$$p_{ij}^{up} = \frac{\rho_i - \rho_{N_{ij}}}{\|\mathbf{A_iN}_{ij}\|}$$

Let us now introduce the mesh parameter

$$\alpha = \min_{1\leqslant i\leqslant I, j\in\mathcal{V}(i)} \frac{\|A_iA_j\|}{\|A_iQ_{ij}\|}.$$

We assume moreover that:

$$\forall 1 \leqslant i, \quad j \leqslant I, \quad i\neq j, \quad Q_{ij} \in]A_i, A_j[, \tag{37}$$

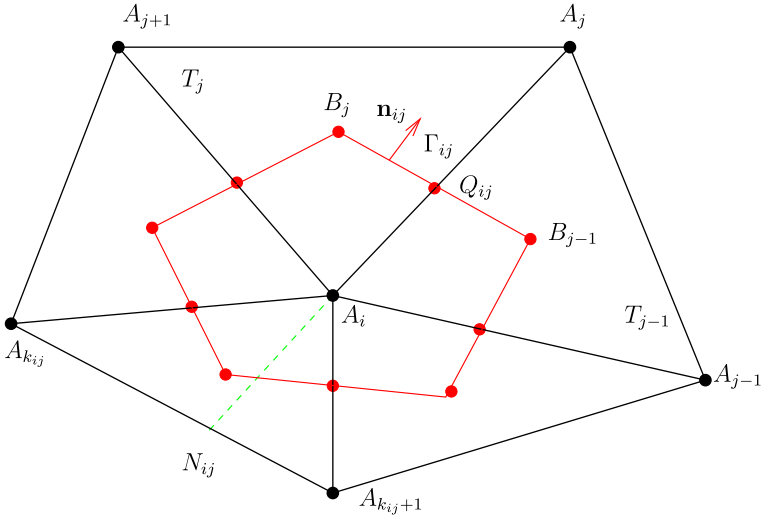

Fig. 3. Construction of the dual mesh: control volume CV2 around the node A_i.

so that $1 \leqslant \alpha \leqslant 2$, with the property that the more regular the mesh, the closer α to 2. Reproducing the arguments used with the CV1 control volume, and assuming that the limiter verifies

$$\forall r \in \mathbb{R}_*^+, \Psi(r) \leqslant \min(\alpha r, \tau) \tag{38}$$

instead of (23), the scheme can be proved to satisfy the local maximum property under the mesh assumption (37) and the CFL:

$$\Delta t \leqslant \min_{1 \leqslant i \leqslant I} \frac{|\mathcal{C}_i|}{\|\mathbf{u}\|_{i,\infty}\left(1 + \frac{\tau C_{\mathcal{T}_h}}{\alpha}\right)\sum_{j \in \mathcal{V}(i)} |\Gamma_{ij}|}. \tag{39}$$

Clearly (39) is equivalent to (27) and even less restrictive in the case $\alpha \geqslant 12/7$. Otherwise, it needs restrictions on the mesh quality, expressed in condition (37). For this reason the CV1 control volume has theoretically to be preferred in the case of fully unstructured meshes.

Remark 4. In the particular case mentioned in Remark 3, the CFL becomes

$$\Delta t \leqslant \frac{3h}{4(\sqrt{2} + 2\sqrt{5})\|\mathbf{u}\|} \approx \frac{h}{7.8\|\mathbf{u}\|}. \tag{40}$$

However there are also some drawbacks with the CV2 construction. Firstly, the node Q_{ij} does not stand in the middle of $[B_{j-1}B_j]$. Consequently, the new density computation:

$$\rho_i^{n+1} = \rho_i^n - \frac{\Delta t}{|\mathcal{C}_i|} \sum_{j \in \mathcal{V}(i)} |\Gamma_{ij}| G_{ij}((\rho_{ij})^n, (\rho_{ji})^n), \tag{41}$$

where the right hand side of (41) is as previously evaluated using an upstream flux:

$$G_{ij}(\rho_1, \rho_2) = \begin{cases} \rho_1 \mathbf{u}_{ij} \cdot \mathbf{n}_{ij} & \text{if } \mathbf{u}_{ij} \cdot \mathbf{n}_{ij} \geqslant 0, \\ \rho_2 \mathbf{u}_{ij} \cdot \mathbf{n}_{ij} & \text{if } \mathbf{u}_{ij} \cdot \mathbf{n}_{ij} < 0, \end{cases} \tag{42}$$

does not correspond to a second-order accuracy numerical integration scheme. Secondly, we have to define the quantity $\mathbf{u}_{ij}$, corresponding to the discrete value of the velocity field at Q_{ij}. A possible determination of this quantity uses the reasoning made for the CV1 case with a suitable interpolation of the values of $\mathbf{u}_{ij}^+$ and $\mathbf{u}_{ij}^-$, corresponding respectively to the discrete values at nodes A_{ij}^+ and A_{ij}^- (see Fig. 1). Anyway, we require to satisfy the consistency constraint

$$\sum_{j \in \mathcal{V}(i)} |\Gamma_{ij}| G_{ij}(\rho_c, \rho_c) = 0. \tag{43}$$

It leads to further computational costs, as well as a loss of accuracy in the discrete velocity field which can affect the global scheme accuracy.

There is no theoretical difficulties in extending the construction of both CV1 and CV2 schemes to the three-dimensional framework. The CV1 construction will be free of geometrical constraint, but in practice the implementation of the scheme and the management of the complex geometry of the control volumes will be very involved. Again, the CV2 construction will be simpler. Nevertheless, it will not be possible by using generic mesh generation to respect the geometrical constraint that guarantees the maximum principle. However, ideas from [16,3] can be adapted to deal with the few "bad" control volumes.

In Section 4, the construction CV1 and CV2 will be tested to analyze and compare their behaviors, as well to confirm the theoretical considerations.

4. Numerical results

In this section we present several numerical tests. We start by dealing with given velocity fields in order to discuss the quality of the approximation. Then, we consider the incompressible Navier–Stokes system and we show the ability of the scheme to deal with large density variation. The simulations are performed on unstructured meshes such as the one displayed in Fig. 4, possibly with refinement strategies (only in Sections 4.2.2 and 4.3, for which meshes are displayed below).

Throughout this section the tiling of the domain is made by using usual conforming and isotropic unstructured meshes composed of triangles, associated to either CV1 or CV2 control volumes, generated by the BAMG software [1], for which the value of h_{min} has to be specified. It allows in particular to avoid triangles with too small angles and all the geometric constants involved in the stability analysis remain controlled. For each mesh considered, the time step is fixed at $\Delta t = 0.2 h_{min}/\|\mathbf{u}\|_\infty$, with h_{min} the size of the smallest edge of the mesh (see in Table 1 the values of Δt when $\|\mathbf{u}\|_\infty = 1$). We first note that for all the following tests, this choice of CFL condition is sufficiently small to numerically ensure the maximum principle, even if it is far less restrictive than the one expected by the theory. Indeed, it is possible to chose a larger Δt than the one given by (27) or (39) according to the control volumes type CV1 or CV2 used, while preserving the maximum principle.

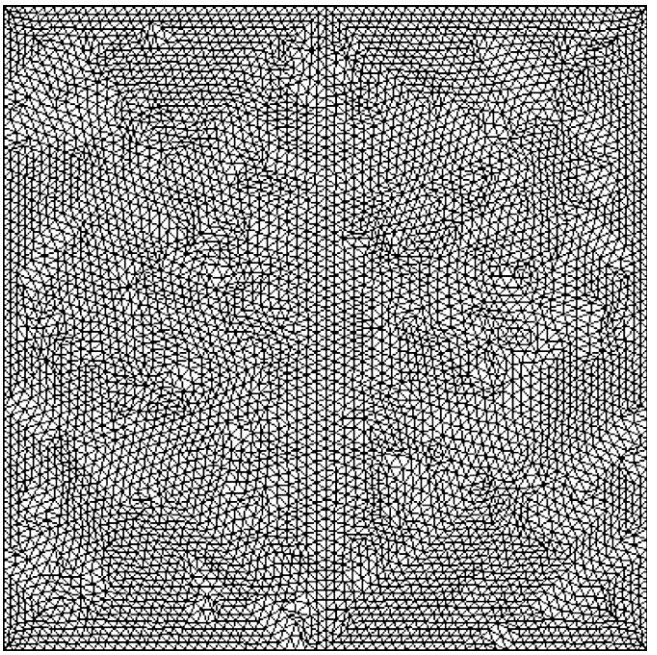

Fig. 4. Example of unstructured mesh used without any adaptive process: level 1.

Table 1
Time-step values with $\|\mathbf{u}\|_\infty = 1$.

Mesh level	h_{min}	Δt
1	4.42E−02	8.84E−03
2	2.21E−02	4.42E−03
3	1.10E−02	2.21E−03
4	5.50E−03	1.10E−03
5	2.76E−03	5.52E−04

For all the simulations presented below, we use the minmod limiter and, concerning time discretization, we actually make use of a second-order in time scheme, based on a natural Runge–Kutta extension of the method discussed in the previous sections.

4.1. Translated field

The first numerical test consists in a convected profile on $\Omega =]-1,1[^2$, with a constant velocity field $\mathbf{u} = (\lambda,\lambda)^T$, where $\lambda = 0.5$. For the initial condition $\rho(t = 0,\mathbf{x}) = \rho_0(\mathbf{x})$, two different functions are used. First, a regular function:

$$\rho_0 = \begin{cases} 0.5(1+\cos(4\pi r)) & \text{if } r \leqslant 0.25, \\ 0 & \text{otherwise}, \end{cases} \tag{44}$$

and then a discontinuous one:

$$\rho_0 = \begin{cases} 1 & \text{if } r \leqslant 0.25, \\ 0 & \text{otherwise}. \end{cases}$$

Setting $r = \sqrt{(x_1+0.25)^2 + (x_2+0.25)^2}$, the initial solutions are centered at the point $(-0.25,-0.25)$. The computations are performed until the final time $t = 1$.

Tables 2 and 3 list the order of the errors in the $L^1(\Omega)$ norm and in the $L^\infty(\Omega)$ norm between the exact solution and the approximation at the final time $t = 1$, computed respectively by:

$$\sum_{A_i \in \mathcal{T}_h} |\mathcal{C}_i||\rho_i - \rho_{exact}(A_i)| \quad \text{and} \quad \max_{A_i \in \mathcal{T}_h} |\rho_i - \rho_{exact}(A_i)|.$$

When a regular function is used, the $L^1(\Omega)$ rate of convergence is very good (namely $\mathcal{O}(h^{1.77})$ for CV1 and CV2 control volumes between the two most refined meshes), and seems to be better than in the cell-centered case [16]. Otherwise, a lower

Table 2
Translation of a regular function: order of the errors for various control cell and meshes.

Mesh level	1–2	2–3	3–4	4–5
L^1 in CV1	1.62	1.52	1.69	1.77
L^1 in CV2	1.65	1.60	1.76	1.77
L^∞ in CV1	0.848	1.17	1.20	1.21
L^∞ in CV2	0.878	1.20	1.20	1.22

Table 3
Translation of a discontinuous function: order of the errors for various control cell and meshes.

Mesh level	1–2	2–3	3–4	4–5
L^1 in CV1	0.61	0.60	0.63	0.62
L^1 in CV2	0.67	0.65	0.67	0.63

rate of convergence is achieved when a discontinuous function translates, leading to similar results than those obtained in [9,16].

Qualitatively, 10 equidistributed isovalues of the density between $\rho = 0.01$ and $\rho = 0.8$ are displayed at initial and final times, for the regular density (Fig. 5) as well as for the discontinuous one (Fig. 6) on the mesh corresponding to mesh level 5 (see Table 1). Since control volumes type CV1 and CV2 give very similar results, only results obtained with CV1 volumes are displayed. For the regular solution, the numerical diffusion is quite small, as expected with a second-order accuracy scheme. For the discontinuous one, the radial symmetry is well preserved.

Finally, we consider a structured mesh like the one considered in Remarks 3 and 4, composed of 256×256 nodes. The initialization is made with the discontinuous solution, and we are looking at the solution obtained after only one iteration in time, according to the time-step value Δt which is no more equal to $0.2h_{min}/\|u\|_\infty$. We are particularly interested in the largest value of Δt for which the maximum principle is still ensured. With the CV1 control volumes, this value is equal to 7.80E−03, compared to 8.3E−03 for the CV2 control volumes. On the one hand, it can be observed that these values are significantly larger than the one given by the theory (respectively 3.1E−04 from (36) for CV1 and 5.0 E−04 from (40) for CV2). On the other hand, it also shows that the use of the CV2 volume control leads to a slightly less restrictive CFL condition, as expected by the theory.

4.2. Rotational field

4.2.1. Convergence rates

The second numerical test consists of a convected profile on $\Omega =]-1,1[^2$, with a stationary rotating velocity field $\mathbf{u} = (-x_2, x_1)^T$. For the initial condition $\rho_0(\mathbf{x})$, the previous regular and discontinuous functions are used, using now $r = \sqrt{x_1^2 + (x_2 + 0.5)^2}$. In this case, the continuous as well as the discrete velocity fields verify the divergence free constraint $\mathrm{div}_{\mathbf{x}}\mathbf{u} = 0$ and, consequently, the numerical scheme uses the consistency property (14) or (43) according to the finite control volume used.

As above, Tables 4 and 5 list the order of the errors in the $L^1(\Omega)$ norm (eventually in the $L^\infty(\Omega)$ norm too) between the exact solution and the approximation at the final time $t = 1.50$. We observe that the rate of convergence is nearly the same using control volumes CV1 or CV2 for the regular function (around $\mathcal{O}(h^{1.80})$ in the $L^1(\Omega)$ norm between the two most refined

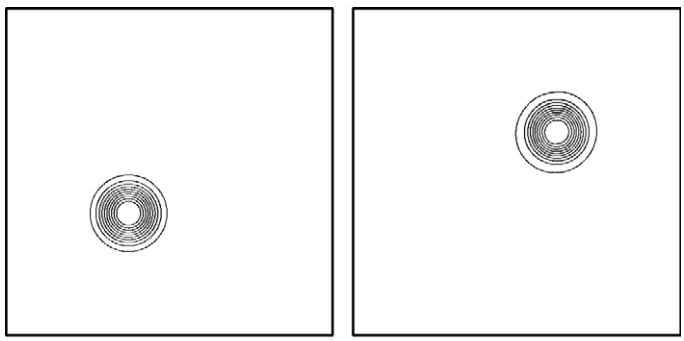

Fig. 5. Density contours of a regular function at $t = 0$ (left) and $t = 1$ (right).

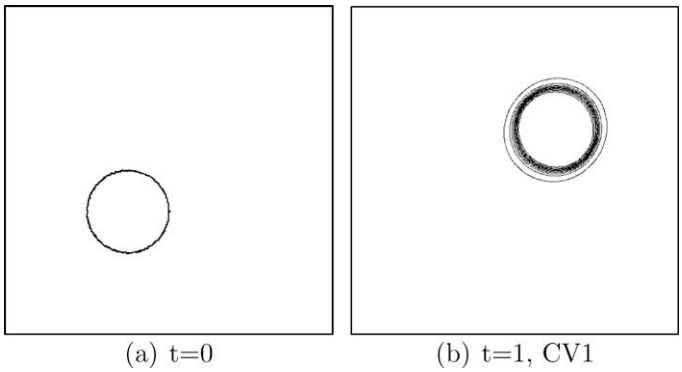

Fig. 6. Density contours of a discontinuous function at $t = 0$ (left) and $t = 1$ (right).

Table 4
Rotation of a regular function: order of the errors for various control cell and meshes, $t = 1.50$.

Mesh level	1–2	2–3	3–4	4–5
L^1 in CV1	1.36	1.62	1.52	1.78
L^1 in CV2	1.47	1.71	1.67	1.82
L^∞ in CV1	0.89	1.15	1.20	1.26
L^∞ in CV2	1.00	1.27	1.19	1.26

Table 5
Rotation of a discontinuous function: order of the errors for various control cell and meshes, $t = 1.50$.

Mesh level	1–2	2–3	3–4	4–5
L^1 in CV1	0.61	0.63	0.65	0.62
L^1 in CV2	0.67	0.64	0.66	0.64

meshes). Moreover, these convergence rates are as good as in the constant velocity field case. Concerning the discontinuous function, results are once again similar for both control volumes.

Once again, 10 equidistributed isovalues of the density between $\rho = 0.01$ and $\rho = 0.8$ are displayed at initial and final times in Fig. 7 (resp. Fig. 8) when a regular density (resp. a discontinuous density) is convected by the rotating velocity field. The views of both control volumes CV1 and CV2 are very similar, then only the first one is displayed.

Remark 5. Let us note that according to the regularity of the initial datum and to the flux limiter function involved, these results can still be a little bit improved. On the one hand, using the $C^\infty(\Omega)$ profile $\rho_0 = e^{-20r^2}$ instead of (44) leads to a better convergence rate in the $L^1(\Omega)$ norm between the two last meshes, respectively 1.92 and 2.02 for the translated and rotational

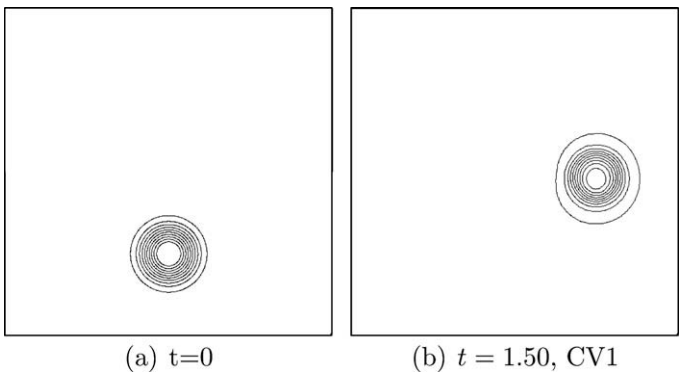

Fig. 7. Density contours of a regular function at $t = 0$ (left) and $t = 1.50$ (right).

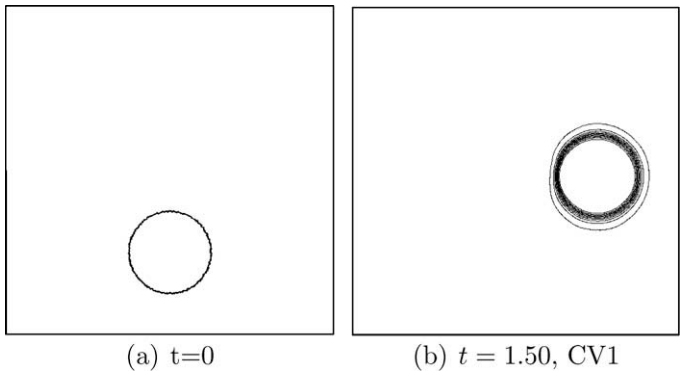

Fig. 8. Density contours of a discontinuous function at $t = 0$ (left) and $t = 1.50$ (right).

fields. Nevertheless, the convergence rate in the $L^{\infty}(\Omega)$ norm remains unchanged (around 1.25 for both cases). On the other hand, using the modified Van-Leer flux limiter (24) instead of the classical minmod one slightly increases the convergence rates, as theoretically expected (0.66 compared to 0.62 for the rotational case in the $L^{1}(\Omega)$ norm).

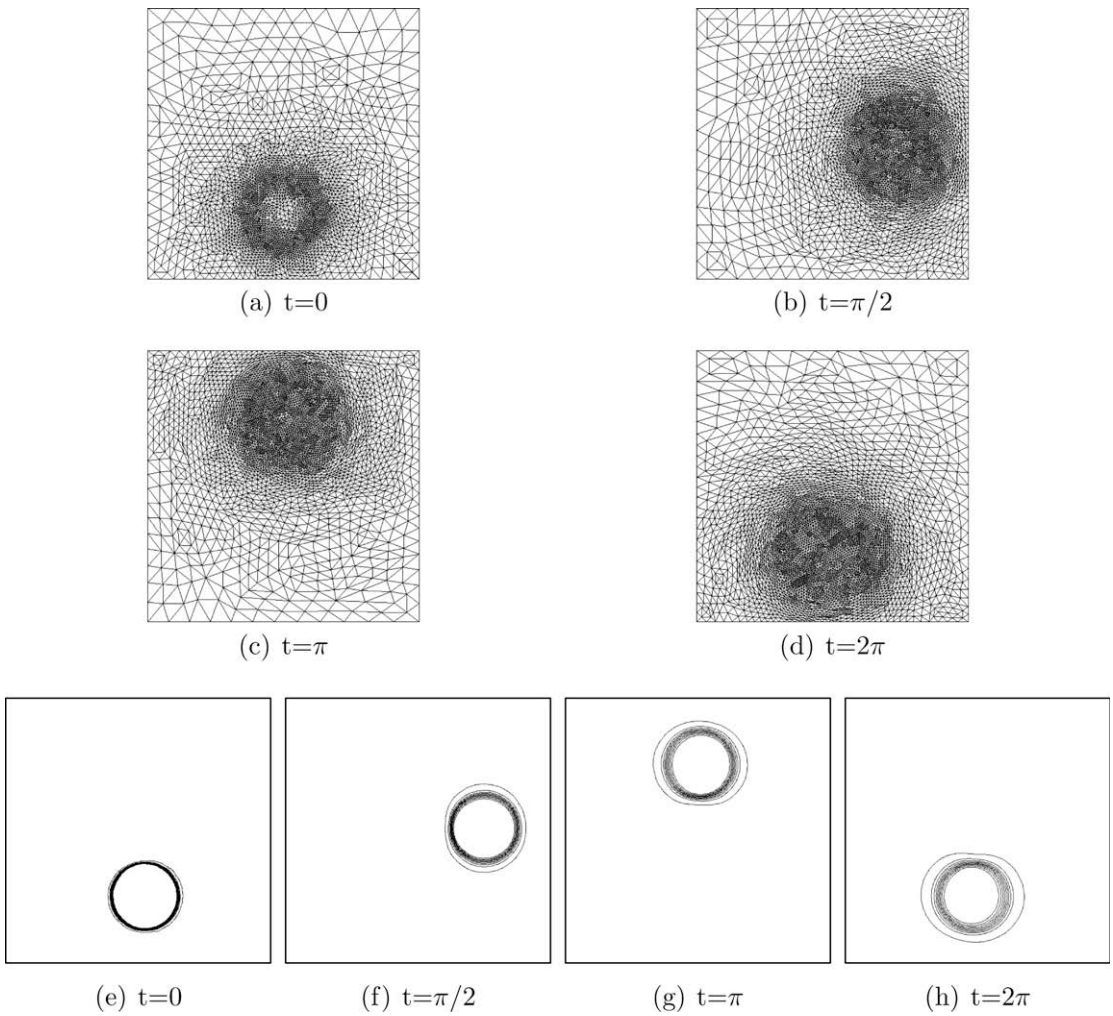

Fig. 9. Mesh (top) and density contours (bottom) of a discontinuous function at $t = 0$, $t = \pi/2$, $t = \pi$ and $t = 2\pi$ with refinement strategy, CV1 control volumes.

4.2.2. Adaptive mesh refinement process

The last test about the rotational field is devoted to the use of the local refinement mesh strategy. It takes advantage of the ability of the scheme in maintaining the local maximum property on fully unstructured meshes. This isotropic mesh-refinement process is based on the BAMG software [1]. Practically, at each $(\Delta t)_{mesh}$ step with $(\Delta t)_{mesh} = 15\Delta t$, the new adapted mesh is built using the previous one as well as the value of the density. This is a very suitable way to detect the density discontinuity lines, and to indicate to the remeshing algorithm where the smallest triangles have to be located. Even if BAMG allows anisotropic mesh generation with the use of the metric concept [26], only the isotropic one is used in the context of this paper. Fig. 9 displays the mesh as well as the isovalues of the density for the discontinuous function at several times of the simulation. Here the final time used is $t = 2\pi$. We obtain the same $L^1(\Omega)$ error on the density than the one obtained in the non-locally refined case by using only 8000 points in the mesh compared to 77,000 points.

4.3. Falling droplet

The goal of this test is to investigate the effectiveness of the proposed scheme by simulating variable density incompressible flows, in the context of very high density ratio such as a water bubble falling in air. This benchmark is already described in [11], but only with a moderate density ratio (namely 100) and a tensorial Cartesian mesh, for which the maximum principle property is simply ensured by the use of a one-dimensional limiter. An unstructured mesh coupled to a local mesh refinement strategy allows far less degrees of freedom for a better accuracy. The scheme is therefore an alternative to

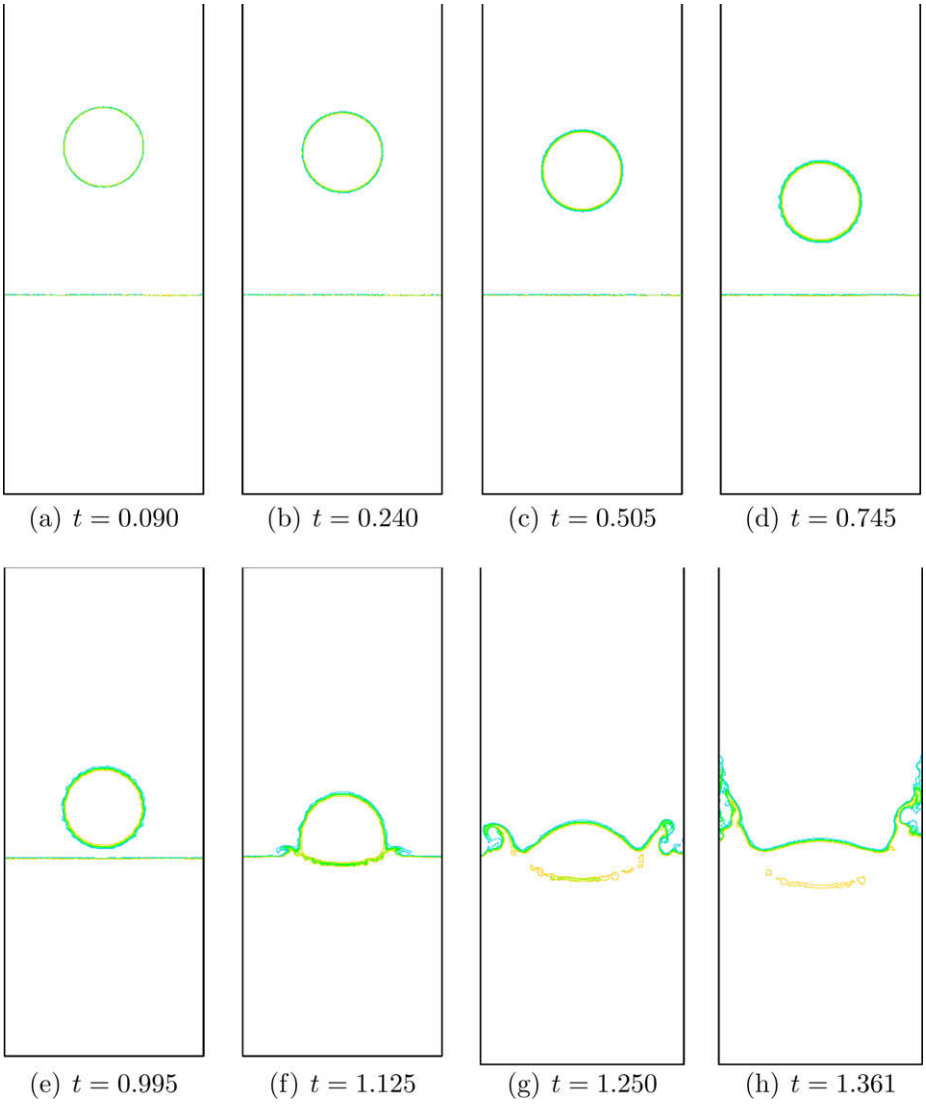

Fig. 10. $\rho_M = 1000$, $h_{min} = 1/400$, density contours = [200, 350, 400, 450, 500, 550, 600, 650, 800].

Cartesian mesh flow solvers to simulate complex flows where the interfaces evolve in less predictable domains, as for instance Rayleigh–Taylor instabilities. Very small triangles can then be concentrated in the close vicinity of the interface, leading to a far smaller global number of degrees of freedom for a given accuracy. Here, a high density ratio is considered. The use of the limiting process described above for the vertex-based finite volume scheme is absolutely essential to provide physical as well as stable simulations. A heavy "droplet" falls through a light fluid and impacts the flat surface of the heavy fluid in a cavity. The computational domain is $(0,d)\times(0,2d)$, where $d=1$ and at $t=0$ the fluid is at rest with density:

$$\rho(x,y)=\begin{cases}\rho_M=1000 & \text{if } 0\leqslant y\leqslant 1 \text{ or } 0\leqslant r\leqslant 0.2,\\ \rho_m=1 & \text{if } 1<y\leqslant 2 \text{ or } 0.2<r,\end{cases}$$

where $r=\sqrt{(x-0.5)^2+(y-1.75)^2}$. As in [40], the equations are made dimensionless by using the following references: ρ_m for density, d for length, $\sqrt{d/G}$ for time, so that the reference velocity is $\sqrt{dG}$. In the dimensionless equations, the gravity term is $\mathbf{f}=(0,-\rho)$ and the Reynolds number is defined by $Re=\frac{\rho_m d^{3/2}G^{1/2}}{\mu}$. In our test, the viscosity of the fluid is supposed to be constant in the whole domain and we have $Re=3132$. The difficulty obviously comes from the very strong discontinuity at the interface. At initial time, the mesh is adapted to the initial condition using the BAMG mesh-refinement procedure [1], associated to the density gradient in order to detect the zones that need to be locally refined. Then, during the simulation, the time frequency of the remeshing process mainly depends on the quantity $\|\mathbf{u}\|_\infty h_{min}$, where $|\mathbf{u}\|_\infty$ is the $L^\infty(\Omega)$ norm of the discrete velocity field, and h_{min} the length of the smallest edge in the mesh. At each remeshing step, once the new mesh is obtained, the old velocity field $\mathbf{u}^{old}$ is not only linearly interpolated on the new mesh, leading to a new discrete field $\mathbf{u}^*$, but also projected on the discrete divergence-free space in order to obtain the velocity field $\mathbf{u}^{new}$ on the new mesh. This is a crucial point to ensure (14), and so to make the finite volume scheme maximum principle preserving. Numerically, it consists in

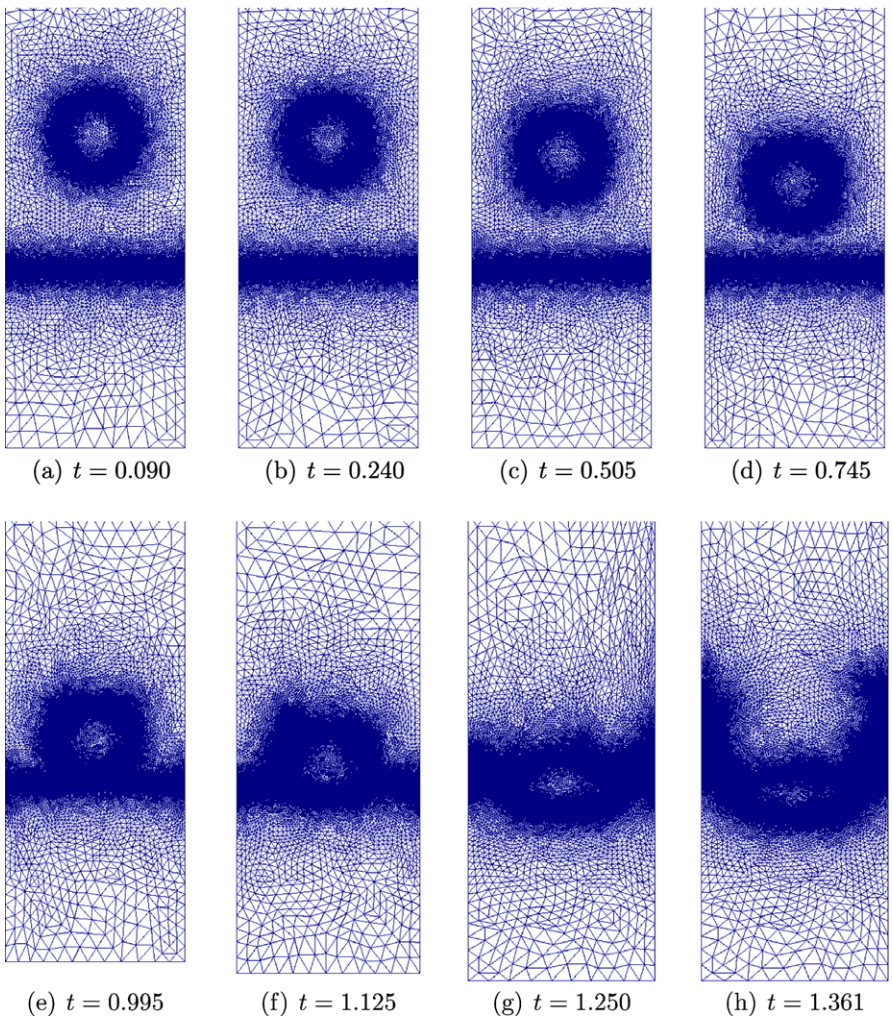

Fig. 11. $\rho_M=1000$, $h_{min}=1/400$, meshes.

the minimization of $||\mathbf{u}^* - \mathbf{u}^{new}||_{L^2(\Omega)}$ under the constraint that $\mathbf{u}^{new}$ is divergence-free from the finite element point of view. It leads to the resolution of a classical saddle-point problem.

For this computation, we use the CV1 mesh and the smallest edge in the mesh is $h_{min} = 1/400$, so that the number of nodes in the mesh evolves from 15,000 to 21,000 during the simulation. Several density isovalues are displayed in Fig. 10 and the corresponding meshes in Fig. 11. The maximum principle is perfectly ensured, and results are very consistent with those of [7,38,40] in slightly different contexts. Note also that these references make use of regular Cartesian grids. After the splash of the droplet, some areas of lighter density contours appear within the heavy fluid, corresponding to a phenomenon for which some particles of lighter fluid are trapped in the heavy fluid after the splash. The change of topology can be clearly distinguished since the two independent regions are merging. The formation of water waves resulting from the splash moving toward the walls can also be remarked. We point out that both the computation and the mesh generation do not exploit the natural symmetries of the problem. Accordingly, some small discrepancies indicating a loss of symmetry can appear, in particular after the splash (see (f), (g), (h) in Fig. 10 and Fig. 11). It could be easily fixed by constructing "manually" a symmetric mesh. Let us note that a difficulty, compared to smaller density ratios, lies in the bad condition number of the linear system (6) and (7) in the finite element step of the algorithm. This feature has to be taken into account in order to actually ensure a discrete divergence-free velocity field, which is a fundamental assumption to provide the stability of the finite volume scheme. To obtain this satisfactory convergence process, the value of h_{min} has so to be chosen sufficiently small according to the value of ρ_M, and a suitable preconditioning strategy has to be used (we refer to [10] for progress in this direction).

5. Conclusion

In this paper, a L^∞-stable MUSCL vertex-based finite volume scheme is developed using a multi-dimensional slope limiter. On the one hand, it is proved to preserve a local maximum principle property under a given Courant–Friedrichs–Levy condition. On the other hand, the proof of the maximum principle is obtained for any discrete divergence-free velocity field, generalizing the constant velocity field case. According to the chosen control volume, two variants are derived. For the first one (namely, the CV1 case), and by contrast to the cell-center finite volume case, the L^∞ stability can be obtained without any geometry restriction on the mesh. The CV2 case we propose is simpler to implement and provides comparable results, but it also implies more constraints on the mesh. Numerical tests on several classical benchmarks lead to very satisfactory convergence rates. The proposed finite volume scheme is incorporated in a more complete code to simulate the evolution of variable density flows with very high density ratios on unstructured meshes, combined to a local mesh refinement strategy.

References

[1] Bamg mesh generator. Available from: <http://pauillac.inria.fr/cdrom/prog/unix/bamg/fra.htm>.
[2] R. Abgrall, P.L. Roe, High order fluctuation schemes on triangular meshes, J. Scient. Comput. 19 (1–3) (2003) 3–36.
[3] G. Ansanay-Alex, Un schéma éléments finis non-conformes/volumes finis pour l'approximation en maillages non structurés des écoulements à faible nombre de Mach. PhD thesis, Université de Provence, Aix-Marseille, France, 2009.
[4] T. Barth, M. Ohlberger, Finite volume methods: foundation and analysis, in: E. Stein, R. de Borst, T. Hugues (Eds.), Encyclopedia of Computational Mechanics, vol. 1, John Wiley & Sons, Ltd, Chichester, 2004, pp. 439–474.
[5] T.J. Barth, D.C. Jespersen. The design and application of upwind schemes on unstructured meshes. In 27th AIAA Aerospace Sciences Meeting, Reno, NV. AIAA, 1989. 1989-0366.
[6] P. Batten, C. Lambert, D.M. Causon, Positively conservative high-resolution convection schemes for unstructured elements, Int. J. Numer. Methods Eng. 39 (11) (1996) 1821–1838.
[7] F. Boyer, A theoretical and numerical model for the study of incompressible mixture flows, Comput. Fluids 31 (1) (2002) 41–68.
[8] C.H. Bruneau, P. Rasetarinera, A finite volume method with efficient limiters for solving conservation laws, J. Comput. Fluid Dyn. 6 (1) (1997) 23–38.
[9] T. Buffard, S. Clain, Monoslope and multislope MUSCL methods for unstructured meshes, J. Comput. Phys. 229 (10) (2010) 3745–3776.
[10] C. Calgaro, J.-P. Chehab, Y. Saad, Incremental incomplete LU factorizations with applications to time-dependent PDEs, Technical report, Minnesota Supercomputer Institute, University of Minnesota, Minneapolis, MN, 2008, Report umsi-2008-276.
[11] C. Calgaro, E. Creusé, T. Goudon, An hybrid finite volume-finite element method for variable density incompressible flows, J. Comput. Phys. 227 (9) (2008) 4671–4696.
[12] C. Chainais-Hillairet, Second order finite volume schemes for a nonlinear hyperbolic equation: error estimate, Math. Methods Appl. Sci. 23 (2000) 467–490.
[13] I. Christov, B. Popov, New nonoscillatory central schemes on unstructured triangulations for hyperbolic systems of conservation laws, J. Comput. Phys. 227 (2008) 5736–5757.
[14] P.G. Ciarlet, The finite element method for elliptic problems, vol. 40 of Classics in Applied Mathematics, Society for Industrial and Applied Mathematics (SIAM), Philadelphia, PA, 2002, Reprint of the 1978 original, North-Holland, Amsterdam.
[15] S. Clain, V. Clauzon, L$^\infty$ stability of the MUSCL methods, Numer. Math. Available as a preprint of the Laboratoire de Mathématiques Appliquées UMR 6620 CNRS–Université Blaise Pascal Clermont-Ferrand II `hal-00329588`.
[16] V. Clauzon, Analyse des schémas d'ordre élevé pour les écoulements compressibles. Application à la simulation numérique d'une torche à plasma. PhD thesis, Université Blaise-Pascal Clermont-Ferrand II, France, 2008.
[17] B. Cockburn, C. Johnson, Shu, C.-W., E. Tadmor, Advanced numerical approximation of nonlinear hyperbolic equations, vol. 1697 of Lecture Notes in Mathematics. Springer-Verlag, Berlin, 1998, Papers from the C.I.M.E. Summer School held in Cetraro, June 23–28, 1997, Edited by Alfio Quarteroni, Fondazione C.I.M.E.
[18] F. Delarue, F. Lagoutière, Probabilistic analysis of the upwind scheme for transport equations, Arch. Rat. Mech. Anal. Available as a preprint of the Laboratoire J.-L. Lions, UMR 7598 CNRS–Université Paris VI, R07060 `hal-00199856`.
[19] A. Dervieux, J.-A. Desideri, Compressible flow solvers using unstructured grids, Technical report, INRIA, 1992, RR–1732.
[20] B. Després, An explicit a priori estimate for a finite volume approximation of linear advection on non-cartesian grids, SIAM J. Numer. Anal. 42 (2) (2004) 484–504.
[21] B. Després, Lax theorem and finite volume schemes, Math. Comput. 73 (247) (2004) 1203–1234.

[22] B. Després, E. Labourasse, F. Lagoutière, The Vofire method for multicomponent flows on unstructured meshes, Technical report, Laboratoire Jacques-Louis Lions, Université Pierre et Marie Curie, Paris 6, France, 2007, R0705.
[23] B. Després, F. Lagoutière, Generalized Harten formalism and longitudinal variation diminishing schemes for linear advection on arbitrary grids, Math. Mod. Numer. Anal. (M2AN) 35 (6) (2001) 1159–1183.
[24] L.J. Durlofsky, B. Engquist, S. Osher, Triangle based adaptive stencils for the solution of hyperbolic conservation laws, J. Comput. Phys. 98 (1992) 64–73.
[25] L. Fezoui, S. Lanteri, B. Larrouturou, C. Olivier, Résolution numérique des équations de Navier–Stokes pour un fluide compressible en maillage triangulaire, Technical report, INRIA, 1989, RR–1033.
[26] P.J. Frey, F. Alauzet, Anisotropic mesh adaptation for CFD computations, Comput. Methods Appl. Mech. Eng. 194 (2005) 5068–5082.
[27] J.B. Goodman, R.J. LeVeque, On the accuracy of stable schemes for 2D conservation laws, Math. Comp. 45 (171) (1985) 15–21.
[28] J.-L. Guermond, L. Quartapelle, A projection FEM for variable density incompressible flows, J. Comput. Phys. 165 (1) (2000) 167–188.
[29] A. Harten, High resolution schemes for hyperbolic conservation laws, J. Comput. Phys. 49 (1983) 357–393.
[30] M.E. Hubbard, Multidimensional slope limiters for MUSCL-type finite volume schemes on unstructured grids, J. Comput. Phys. 155 (1) (1999) 54–74.
[31] R.J. LeVeque, Numerical methods for conservation laws. Lectures in Mathematics ETH Zürich, second ed., Birkhäuser Verlag, Basel, 1992.
[32] D.W. Levy, M.D. Thacker, Comparison of unstructured cell- and node-based schemes for the euler equations, in: 17th AIAA Applied Aerodynamics Conference, Norfolk, VA, AIAA, June 1999, pp. 1999-3185.
[33] X.D. Liu, A maximum principle satisfying modification of triangle based adaptive stencils for the solution of scalar hyperbolic conservation laws, SIAM J. Numer. Anal. 30 (3) (1993) 701–716.
[34] D. Mavriplis, Unstructured mesh discretizations and solvers for computational aerodynamics, in: 18th AIAA Computational Fluid Dynamics Conference, Miami, FL, AIAA, June 2007, pp. 2007–3955.
[35] B. Merlet, Error estimate for the finite volume scheme applied to the linear advection equation, SIAM J. Numer. Anal. 46 (1) (2007/08) 124–150.
[36] B. Merlet, J. Vovelle, Error estimate for finite volume scheme, Numer. Math. 106 (1) (2007) 129–155.
[37] S. Osher, Convergence of generalized MUSCL schemes, SIAM J. Numer. Anal. 22 (5) (1985) 947–961.
[38] G.P. Puckett, A.S. Almgren, J.B. Bell, D.L. Marcus, W. Rider, A high-order projection method for tracking fluid interfaces in variable density incompressible flows, J. Comput. Phys. 130 (2) (1997) 269–282.
[39] P.L. Roe, Generalized formulation of TVD Lax-Wendroff schemes, Technical report, NASA Langley Research Center, Hampton, VA, 1984, ICASE Report 84-53.
[40] T. Schneider, N. Botta, K.J. Geratz, R. Klein, Extension of finite volume compressible flow solvers to multidimensional variable, density zero Mach number flows, J. Comput. Phys. 155 (1999) 248–286.
[41] C.W. Shu, Numerical experiments on the accuracy of ENO and modified ENO schemes, J. Scient. Comput. 5 (1990) 127–149.
[42] G. Strang, On the construction and comparison of difference schemes, SIAM J. Numer. Anal. 5 (1968) 506–517.
[43] P.K. Sweby, High resolution schemes using flux limiters for hyperbolic conservation laws, SIAM J. Numer. Anal. 21 (5) (1984) 995–1011.
[44] B. Van Leer, Towards the ultimate conservative difference scheme V. A second-order sequel to Godunov's method, J. Comput. Phys. 32 (1979) 101–136.
[45] B. Van Leer, On the relation between the upwind-differencing schemes of Godunov, Engquist–Osher and Roe, SIAM J. Sci. Stat. Comput. 5 (1) (1984) 1–20.
[46] H.C. Yee, Construction of explicit and implicit symmetric TVD schemes and their applications, J. Comput. Phys. 68 (1987) 151–179.